

# Reconstructing the Cosmic Velocity and Tidal Fields with Galaxy Groups Selected from the Sloan Digital Sky Survey

Huiyuan Wang<sup>1,2\*</sup>, H.J. Mo<sup>3</sup>, Xiaohu Yang<sup>4</sup> and Frank C. van den Bosch<sup>5</sup>

<sup>1</sup>*Key Laboratory for Research in Galaxies and Cosmology, University of Science and Technology of China, Hefei, Anhui 230026, China*

<sup>2</sup>*Department of Astronomy, University of Science and Technology of China, Hefei, Anhui 230026, China*

<sup>3</sup>*Department of Astronomy, University of Massachusetts, Amherst MA 01003-9305, USA*

<sup>4</sup>*Key Laboratory for Research in Galaxies and Cosmology, Shanghai Astronomical Observatory, Shanghai 200030, China*

<sup>5</sup>*Astronomy Department, Yale University, P.O. Box 208101, New Haven, CT 06520-8101, USA*

Accepted ..... Received .....; in original form .....

## ABSTRACT

Cosmic velocity and tidal fields are important for the understanding of the cosmic web and the environments of galaxies, and can also be used to constrain cosmology. In this paper, we reconstruct these two fields in the Sloan Digital Sky Survey (SDSS) volume from dark matter halos represented by galaxy groups. Detailed mock catalogues are used to test the reliability of our method against uncertainties arising from redshift distortions, survey boundaries, and false identifications of groups by our group finder. We find that both the velocity and tidal fields, smoothed on a scale of  $\sim 2 h^{-1}\text{Mpc}$ , can be reliably reconstructed in the inner region ( $\sim 66\%$ ) of the survey volume. The reconstructed tidal field is used to split the cosmic web into four categories: clusters, filaments, sheets, and voids, depending on the sign of the eigenvalues of local tidal tensor. The reconstructed velocity field nicely shows how the flows are diverging from the centers of voids, and converging onto clusters, while sheets and filaments have flows that are convergent along one and two directions, respectively. We use the reconstructed velocity field and the Zel'dovich approximation to predict the mass density field in the SDSS volume as function of redshift, and find that the mass distribution closely follows the galaxy distribution even on small scales. We find a large-scale bulk flow of about  $117 \text{ km s}^{-1}$  in a very large volume, equivalent to a sphere

with a radius of  $\sim 170 h^{-1}\text{Mpc}$ , which seems to be produced by the massive structures associated with the SDSS Great Wall. Finally, we discuss potential applications of our reconstruction to study the environmental effects of galaxy formation, to generate initial conditions for simulations of the local Universe, and to constrain cosmological models. The velocity, tidal and density fields in the SDSS volume, specified on a Cartesian grid with a spatial resolution of  $\sim 700 h^{-1}\text{kpc}$ , are available from the authors upon request.

**Key words:** dark matter - large-scale structure of the universe - galaxies: haloes - methods: statistical

## 1 INTRODUCTION

The study of the large-scale structure in the universe traditionally relies on large redshift surveys of galaxies, such as the Sloan Digital Sky Survey (hereafter SDSS; York et al. 2000). However, since galaxies are biased tracers of the mass distribution, one has to understand the relationship between galaxies and dark matter before using the galaxy distribution in space to study the mass distribution in the universe. In recent years, tremendous amounts of effort have been put into the establishment of the relationship between galaxies and dark matter halos (the virialized clumps of dark matter clumps). Since the relationship between the distribution of dark matter halos and the mass distribution is well understood (e.g. Mo & White 1996; Jing 1998; Sheth & Tormen 1999; Sheth, Mo & Tormen 2001; Seljak & Warren, 2004; Reed et al. 2009; Pillepich, Porciani & Hahn 2010; Tinker et al. 2010), the galaxy-halo connection then provides an important avenue to investigate the density and velocity fields in the universe from the observed galaxy distribution.

An empirical way to establish the galaxy-halo connection is to use galaxy groups, provided that they are defined as sets of galaxies that reside in the same dark matter halo. Recently, Yang et al. (2005; 2007) have developed a halo-based group finder that is optimized for grouping galaxies residing in the same dark matter halo. Using mock galaxy redshift surveys constructed from the conditional luminosity function model (e.g. Yang, Mo & van den Bosch 2003) and semi-analytical models (Kang et al, 2005), it is found that this group finder is very successful in associating galaxies with their common dark matter haloes. The group finder performs reliably for poor systems, including isolated galaxies in

small mass haloes, making it ideally suited for the study of the relation between galaxies and dark matter haloes over a wide range of halo masses (see also Weinmann et al. 2006 and Wang et al. 2008). These galaxy groups, and the dark haloes they represent, together with the relationship between dark haloes and the mass density field predicted by the current CDM model, offer an unprecedented opportunity to reconstruct the cosmic density and velocity fields in the cosmic volume within which the galaxies are observed.

A powerful reconstruction method will also make it possible to classify the morphology of the large scale structure. Most methods aimed at describing the morphology of the large scale structure are either based directly on the galaxy distribution (e.g. Hoyle & Vogeley 2002; Romano-Díaz & van de Weygaert 2007; Sousbie et al. 2011) or on the smoothed density field (e.g., Park et al. 2005; Aragón-Calvo et al. 2007). A particularly interesting classification is based on the tidal field tensor, which is simply the Hessian of the gravitational potential (e.g. Hahn et al. 2007a,b; Forero-Romero et al. 2009; Aragón-Calvo et al. 2010a,b). Since many properties of dark matter halos are found to be correlated with the large-scale tidal field (e.g. Wang et al. 2011), such a classification is particularly interesting for investigating how galaxy properties are affected by their large-scale environment. Hence, a reconstruction method that yields an accurate estimate of the tidal field will open an important avenue for the study of galaxy formation and evolution.

In an earlier paper (Wang et al. 2009; hereafter W09), we developed a method to reconstruct the cosmic density, velocity and tidal fields starting from the distribution of (massive) galaxy groups (i.e., dark matter haloes), which we tested against  $N$ -body simulations but did not apply to real data. The method to reconstruct the *density* field partitions the volume in domains associated with each individual group (i.e., dark matter halo), and models the mass distribution in each domain using the cross-correlation function between dark matter haloes and the mass distribution within their domain obtained from  $N$ -body simulations. The redshift distortions of the groups (domains) are corrected iteratively by reconstructing the velocity field using linear theory, in which the density field is traced by the most massive groups, as described below. This method is very different from previous methods that have been used in earlier investigations (e.g. Fisher et al. 1995; Zaroubi et al. 1995; Erdoğan et al. 2004). In these studies the galaxy distribution is usually smoothed heavily and normalized to represent the cosmic density field on large scales. In the Wiener reconstruction method, adopted in many of these earlier investigations, the mass density at a given point is assumed to be a linear combination of the observed galaxy density field values at different points

so that the reconstructed field has the minimum mean square error. Therefore the results are expected to be valid only on linear scales. Since our method is based on dark matter haloes, the reconstruction is expected to be more accurate both on small scales, where mass is strongly correlated with dark matter halos (see also Kitauro et al. 2010; Jasche & Kitauro 2010 for other methods to reconstruct the non-linear density field), and on large scales, where the halo bias is well understood.

For the reconstruction of the velocity and tidal fields, W09 used a slightly different method. Since the velocity field is mainly dominated by the mass distribution on large scales, it can be reconstructed simply from the distribution of the massive groups (haloes), without having to account for their cross-correlation with the dark matter in their domains (as we did for the reconstruction of the density field). Using linear theory and a smoothed density field based on the distribution of massive haloes, W09 were able to accurately reconstruct the velocity and tidal fields on large scales. The velocity field thus obtained was used in correcting the reconstructed density field for redshift distortions. This method for reconstructing the cosmic velocity field is different from those used in earlier investigations, which always used the galaxy distribution directly (e.g. Kaiser et al. 1991; Willick & Strauss 1998; Hudson et al. 2004), and therefore suffer from uncertainties in the complicated relation between galaxies and the underlying mass distribution (e.g., the fact that galaxy bias depends on luminosity and color). The advantage of our method is that it is based on dark matter halos, as represented by galaxy groups, so that the bias of the distribution of different galaxies relative to the underlying density field is automatically taken into account by their connections to dark matter halos, whose bias is well understood.

The reconstruction method presented in W09 was recently used by Munoz-Cuartas et al. (2011) to reconstruct the density field for the survey volume of the SDSS DR4 (Adelman-McCarthy et al. 2006), using the SDSS galaxy group catalogue of Yang et al. (2007). However, we caution that Munoz-Cuartas et al. chose not to apply the corrections for redshift distortion; hence their reconstructed density field is in redshift space. In addition, they computed the tidal deformation tensor, but did not properly account for boundary effects of the SDSS volume, which, as we will see in this paper, are very substantial. In this paper, we use the method of W09 to reconstruct the cosmic velocity field and the associated tidal field in the SDSS survey volume. Our analysis differs from that of Munoz-Cuartas et al. (2011) in that (i) we mainly focus on the reconstruction of velocity and tidal fields, (ii) we use the much larger SDSS DR7 (Abazajian et al. 2009) and its corresponding galaxy group catalogue,

(iii) we correct the locations of the groups for redshift distortions, and (iv) we carefully investigate the impact of boundary effects on the accuracy of the reconstructed velocity and tidal fields. To that extent we use detailed mock catalogues to test the reliability of our method against uncertainties arising from redshift distortions, survey boundaries, and false identifications of groups by our group finder. We also present a new, alternative method to reconstruct the density field, which does not require  $N$ -body simulations to obtain the halo-matter cross-correlation in halo domains. Rather, the method uses the reconstructed velocity field and the Zel'dovich (1970) approximation to infer the density field across cosmic times. Note that although this method is much simpler, and less time-consuming, it only yields an estimate of the smoothed density field (i.e., it is unable to resolve highly non-linear regions). Hence, this method should be considered complementary to the method presented in W09, rather than as a true alternative.

This paper is organized as follows. In Section 2 we present the galaxy and group catalogues used in this paper. Section 3 describes our reconstruction method, which is tested against mock galaxy catalogues based on high resolution  $N$ -body simulations in Section 4. The reconstruction results based on the SDSS catalog are presented in Section 5, and we summarize and discuss our findings in Section 6. Throughout this paper we adopt a WMAP5 cosmology (Dunkley et al. 2009): the density parameter  $\Omega_m = 0.258$ ; the cosmological constant  $\Omega_\Lambda = 0.742$ ; the baryon density parameter  $\Omega_b = 0.044$ ; the Hubble constant  $h = 0.72$ ; and the linear  $RMS$  density fluctuation in a sphere of an  $8 h^{-1}\text{Mpc}$  radius,  $\sigma_8$ , equals 0.8.

## 2 THE SDSS CATALOGUE

The galaxy sample used here is constructed from the New York University Value-Added Galaxy Catalogue (NYU-VAGC; Blanton et al. 2005), which is based on SDSS DR7 but includes a set of improved reductions over the original pipeline. We use all galaxies in the Main Galaxy Sample with extinction-corrected apparent magnitudes brighter than  $r = 17.72$ , with redshifts in the range  $0.01 \leq z \leq 0.20$ , and with redshift completeness  $\mathcal{C}_z > 0.7$ . The catalogue contains a total of 639,359 galaxies with a sky coverage of 7,748 square degrees. For each galaxy we compute its stellar mass from the  $g$  and  $r$ -band magnitudes using the method of Bell et al. (2003). DR7 covers two sky regions: a larger region in the Northern Galactic Cap (NGC) and a smaller region in the Southern Galactic Cap (SGC). As we demonstrate later, survey boundaries can significantly impact the accuracy of our

reconstruction, and we therefore only use the more contiguous NGC region (see Fig. 1 for a view of the sky coverage used), which contains 584,473 galaxies with a sky coverage of 7,047 square degrees.

Galaxy groups are selected using the adaptive halo-based group finder developed by Yang et al. (2005). The application of this group finder to the SDSS DR4 is described in detail in Yang et al. (2007; hereafter Y07). The application to SDSS DR7 is exactly the same, except that the sky coverage is significantly larger and we adopt the WMAP5 cosmology, rather than the WMAP3 cosmology used by Y07. The geometry of the SDSS used for the group catalogue is defined as the region on the sky that satisfies the redshift completeness criterion. As described in detail in Y07, our group finder takes account of the survey edges in the SDSS volume by estimating the fraction,  $f_{\text{edge}}$ , of each group’s volume that falls inside of the survey volume. Group luminosities and masses are then corrected for this fraction, and groups with  $f_{\text{edge}} < 0.6$  are excluded, which removes only 1.6% of all groups.

As described in Y07, the majority of the groups in the catalogue have two estimates of their dark matter halo masses: one based on the ranking of the total characteristic luminosities of groups, and the other based on the ranking of the total characteristic stellar masses, both determined from group member galaxies more luminous than  $M_r - 5 \log h = -19.5$ . As shown in Y07, both halo masses agree very well with each other, with an average scatter that decreases from  $\sim 0.1$  dex at the low mass end to  $\sim 0.05$  at the massive end. In this paper we adopt the halo masses based on the characteristic luminosity ranking. The luminosity-based group masses are available for a total of 355,482 groups in our sample, which host a total of 502,651 galaxies. The mass assignment based on characteristic luminosity ranking is complete to  $z \sim 0.12$  for groups with halo masses  $M_h \gtrsim 10^{12} h^{-1} M_\odot$ , and to  $z \sim 0.14$  for  $M_h \gtrsim 10^{12.5} h^{-1} M_\odot$  (see Y07). In our analysis, we will use all groups with  $M_h \geq M_{\text{th}} = 10^{12} h^{-1} M_\odot$  and so we restrict our reconstruction to the nearby volume covering the redshift range  $0.01 \leq z \leq 0.12$ , which we call the survey volume. Within this survey volume, the total number of groups above our mass limit (i.e., with  $M_h \geq M_{\text{th}}$ ) is 12,192. Fig. 1 shows the distribution of these groups (black dots) as well as the distribution of galaxies that are assigned to halos with smaller masses (hereafter ‘field galaxies’, red dots), in a specific redshift slice centered on  $z \sim 0.08$ , chosen to show the SDSS ‘Great Wall’ (Gott et al. 2005). As one sees clearly, the distribution of the field galaxies closely follows the large-scale structure delineated by the more massive groups.

To perform the reconstruction, we transform the redshift distances and J2000.0 coordi-

rates for each group into the following comoving Cartesian coordinates:

$$\begin{aligned} X &= r(z) \cos \delta_J \cos \alpha_J; \\ Y &= r(z) \cos \delta_J \sin \alpha_J; \\ Z &= r(z) \sin \delta_J. \end{aligned} \tag{1}$$

Here  $\alpha_J$  and  $\delta_J$  refer to the J2000.0 right ascension and declination, respectively, and  $r(z)$  is the comoving distance at redshift  $z$ . For the WMAP5 cosmology adopted here, the ranges for  $X$ ,  $Y$  and  $Z$  axes of the survey volume are  $(-351.0, -1.5)$ ,  $(-329.7, 302.0)$  and  $(-22.7, 330.3)$  (in units of  $h^{-1}\text{Mpc}$ ), so the maximal scale along the three axes are about 350, 632, and  $353 h^{-1}\text{Mpc}$ , respectively.

### 3 THE RECONSTRUCTION METHOD

We now describe our method to reconstruct the velocity and tidal fields for the SDSS survey volume. Our method closely follows that of W09, but with a few small modifications that are required in order to properly account for the complicated geometry of the SDSS survey volume.

#### 3.1 Velocity field

In the linear regime, the peculiar velocity can be derived as

$$\mathbf{v} = -\frac{1}{4\pi G \bar{\rho} a} \frac{\dot{D}}{D} \nabla \phi, \tag{2}$$

where  $G$ ,  $a$ ,  $\bar{\rho}$  and  $D$  are the gravitational constant, the scale factor of the universe, the cosmic mean density and the linear growth rate, respectively. The quantity  $\phi$  is the peculiar gravitational potential and can be calculated from the density perturbation ( $\delta$ ) through the Poisson equation:

$$\nabla^2 \phi = 4\pi G \bar{\rho} a^2 \delta. \tag{3}$$

Combining these two equations, and working in Fourier space, we have

$$\mathbf{v}(\mathbf{k}) = H a f(\Omega) \frac{i\mathbf{k}}{k^2} \delta(\mathbf{k}), \tag{4}$$

where  $\mathbf{v}(\mathbf{k})$  and  $\delta(\mathbf{k})$  are the Fourier transforms of  $\mathbf{v}$  and  $\delta$ , respectively,  $H$  is the Hubble constant, and  $f(\Omega) = d \ln D / d \ln a \simeq \Omega_m^{0.6} + \frac{1}{70} \Omega_\Lambda (1 + \Omega_m/2)$  (e.g. Lahav et al. 1991).

As described and demonstrated in W09, one can compute the velocity field using only the density field represented by dark matter haloes above a given mass threshold,  $M_{\text{th}}$ .

The predicted velocity,  $\mathbf{v}_h(\mathbf{x})$ , based on this halo distribution is tightly correlated with, and directly proportional to, the real velocity,  $\mathbf{v}(\mathbf{x})$ . In particular, we can write that (see Colombi, Chodorowski, & Teyssier 2007)

$$\mathbf{v}_h(\mathbf{k}) = \text{Haf}(\Omega) \frac{i\mathbf{k}}{k^2} \delta_h(\mathbf{k}) = b_{\text{hm}} \text{Haf}(\Omega) \frac{i\mathbf{k}}{k^2} \delta(\mathbf{k}) = b_{\text{hm}} \mathbf{v}(\mathbf{k}), \quad (5)$$

where  $\delta_h(\mathbf{k})$  is the Fourier transform of the mass density contrast represented by the haloes with mass  $M_h \geq M_{\text{th}}$ , hereafter  $\delta_h(\mathbf{x})$ . As explicitly shown in W09,  $b_{\text{hm}}$  is the average bias of the haloes with mass  $M_h \geq M_{\text{th}}$ , and therefore the bias of the density field,  $\delta_h$ , is given by

$$b_{\text{hm}} = \frac{\int_{M_{\text{th}}}^{\infty} M b_h(M) n(M) dM}{\int_{M_{\text{th}}}^{\infty} M n(M) dM}, \quad (6)$$

where  $n(M)$  and  $b_h(M)$  are the halo mass function and the halo bias function, respectively. This bias factor can also be obtained through a comparison between the predicted velocities based on dark matter particles and haloes, as was done in W09. Thus, the velocity field can be reconstructed using only the population of haloes above some mass threshold. This is fortunate, since it means that we can use our group catalogue, which represents massive dark matter haloes, to accurately reconstruct the cosmic velocity field.

In order to reconstruct the velocity field in the SDSS survey volume we proceed as follows. We first embed the survey volume in a periodic, cubic box of  $726 h^{-1}\text{Mpc}$  on a side (In the following, this will be referred to as the survey box to distinguish it from the survey volume and the simulation box to be defined below). The linear size of the survey box is chosen to be about  $100 h^{-1}\text{Mpc}$  larger than the maximal scale of the survey volume among the three axes. We divide the box into  $1024^3$  grid cells (which are  $\sim 0.7 h^{-1}\text{Mpc}$  on a side), and sort them into two types: survey grid cells and non-survey grid cells, depending on whether or not the center of the grid cell in question is located inside the survey volume. We assign the mass of each group (with mass  $\geq M_{\text{th}}$ ) on the survey grid according to its redshift-space coordinates. This is done by assuming that the halo mass is distributed homogeneously within a radius of  $R_{200}/2$ , where  $R_{200}$  is the virial radius of the halo. Since we will smooth the density field on relatively large scales, our results are very insensitive to how exactly we distribute the halo mass; for example, we have verified that adopting a Dirac delta function, rather than a top-hat sphere, yields results that are indistinguishable. Non-survey grid cells are assigned a density equal to the average mass density of the groups (with  $M_h \geq M_{\text{th}}$ ) in the survey volume (hereafter  $\bar{\rho}_h$ ) so that the entire survey box has the same mean density as the actual survey volume. Next we compute the overdensity field of our groups (in redshift



space), defined by

$$\delta_{h,i} = \frac{\rho_{h,i} - \bar{\rho}_h}{\bar{\rho}_h} \quad (7)$$

where the index  $i$  refers to the grid cell in question.

To correct for the redshift distortions due to the peculiar velocities of the groups, we follow exactly the procedure developed by W09. We first smooth the density field using a Gaussian smoothing kernel with a mass scale of  $\log(M_s/h^{-1}M_\odot) = 14.75$ , which corresponds to a Gaussian kernel size of

$$R_s \equiv \frac{1}{\sqrt{2\pi}} \left( \frac{M_s}{\bar{\rho}} \right)^{1/3} = 7.93 h^{-1} \text{Mpc} \quad (8)$$

for the WMAP5 cosmology adopted here<sup>1</sup>. Next we Fast Fourier Transform (FFT) the smoothed overdensity field of our groups, and use Eq. (5) to compute  $\mathbf{v}(\mathbf{k}) = \mathbf{v}_h(\mathbf{k})/b_{hm}$ , where  $b_{hm}$  is computed using Eq. (6). Fourier transforming  $\mathbf{v}(\mathbf{k})$  then yields the velocity field, which we use to compute the peculiar velocity-corrected, cosmological redshift of each group according to

$$z_{\text{corr}} = \frac{z_{\text{obs}} - (v_{\text{los}}/c)}{1 + (v_{\text{los}}/c)}, \quad (9)$$

where  $v_{\text{los}}$  is the line-of-sight component of the peculiar velocity and  $z_{\text{obs}}$  is the observed redshift of the group (i.e., the luminosity weighted average redshift of the group members). Since the velocity field is computed using the redshift space distribution of the groups, this method needs to be iterated until convergence is achieved. Detailed tests with mock catalogs suggest that two iterations are generally sufficient. Note that the relatively large smoothing scale is adopted to suppress non-linear velocities that cannot be predicted accurately with our linear model. Thus, our method only corrects redshift distortions in the linear and quasi-linear regime. The choice of a large smoothing scale prevents the iterations from getting trapped in a local minimum. However, the correction is not sufficient in the boundary regions, as we will show below.

Now that we have a sample of groups with corrected positions, we can use the procedure described above to assign group masses on the survey grids to obtain  $\delta_h$  in ‘real space’. In order to obtain the velocity field on different scales, we smooth the density field with several choices of  $M_s$ . The values of  $\mathbf{v}_h/b_{hm}$  on all the grid points then represent the predicted peculiar velocity field.

<sup>1</sup> As tested and described in W09, this is the optimal smoothing scale for the redshift distortion corrections.

### 3.2 Gravitational tidal field

We describe the large-scale tidal field through the tidal tensor,  $\mathcal{T}_{ij}$ , defined as

$$\mathcal{T}_{ij} = \partial_i \partial_j \phi, \quad (10)$$

where  $\phi$  is the peculiar gravitational potential which can be calculated from the mass density field using the Poisson equation [Eq. (3)]. Since we want to derive the tidal field using only haloes (galaxy groups) with mass  $M_h \geq M_{\text{th}}$ , we write the corresponding gravitational potential,  $\phi_h$ , as

$$\nabla^2 \phi_h = 4\pi G \bar{\rho}_h a^2 \delta_h = 4\pi G \bar{\rho} a^2 (b_{\text{hm}} \delta) \left( \frac{\bar{\rho}_h}{\bar{\rho}} \right) = b_{\text{hm}} \frac{\bar{\rho}_h}{\bar{\rho}} \nabla^2 \phi, \quad (11)$$

where  $\delta_h$  is again the mass density distribution of groups with  $M_h \geq M_{\text{th}}$  and  $\bar{\rho}_h$  is the corresponding mean mass density. We thus can derive  $\phi$  and  $\mathcal{T}_{ij}$  using galaxy groups. It is easy to see that the bias factor,  $b_{\text{hm}}$ , in the above equation is the same as that in Eq. (5). The value of  $\delta_h$  can be obtained using exactly the same method as described in Section 3.1, and we smooth  $\delta_h$  with a Gaussian smoothing kernel of a given mass  $M_s$ . We then use FFT to obtain the potential field,  $\phi$ , by solving the Poisson equation, and derivative operators are applied (in Fourier space) to derive the tidal tensors. Finally, the eigenvalues  $T_1$ ,  $T_2$  and  $T_3$  ( $T_1 > T_2 > T_3$ ) of the tidal tensor are obtained at each grid point by diagonalizing the corresponding tidal tensor.

The tidal field impacts dark matter haloes, and their associated baryonic material, with a net angular momentum, and plays an important role in regulating the growth and shape of dark matter haloes (e.g., White 1984; Hahn et al. 2007a,b; Wang et al. 2011). Hence, the tidal field is an important description of the environments in which haloes and galaxies reside. In particular, the number of positive eigenvalues of the tidal tensor can be used to define the morphologies of large scale structures (e.g. Hahn et al. 2007a,b; Forero-Romero et al. 2009; Munoz-Cuartas et al. 2011). If all of the three eigenvalues of a grid cell are positive, the grid cell is classified as **cluster**. Similarly, grid cells with one or two negative eigenvalues are classified as **filament** or **sheet**, respectively, while grid cells for which all three eigenvalues are negative are classified as **void**. It is worthwhile to note that the tidal field is the second derivative of the gravitational potential, while the velocity field is the first derivative. The tidal field is therefore proportional to the derivative of the velocity field and can be used to characterize the convergence and divergence of the flow: around a **cluster** point, the three positive eigenvalues mean that the flows along all directions are converging to that point; around a **filament** point the flow is convergent along two directions but divergent along

the third; around a **sheet** point the flow is convergent along one direction but divergent along the other two; and around a **void** point, the flow is divergent in all directions. All this meshes well with the picture of the cosmic web formation in the current CDM model (e.g. Bond et al. 1996), indicating that the classification of the large-scale structure according to the signs of  $T_1$ ,  $T_2$  and  $T_3$  provides a useful description of the various patterns in the cosmic density and velocity fields.

## 4 TESTS BASED ON MOCK DATA

Before applying our method to the actual SDSS data, we need to gauge the reliability of our reconstruction. Although many tests have already been presented in W09, here we focus specifically on an application to the SDSS survey volume, carefully assessing the impact of boundary effects associated with the complicated geometry of the SDSS survey volume. To that extent we use a mock SDSS group catalogue constructed from  $N$ -body simulations to carry out a series of test to verify the reliability of our method against uncertainties arising from redshift distortion, survey boundaries, and false identifications of groups by our group finder.

### 4.1 The N-body simulation and Mock catalogs

We use the “Millennium Simulation” (MS) carried out by the Virgo Consortium (Springel et al. 2005). This simulation assumes a spatially-flat  $\Lambda$ CDM model, with density parameter  $\Omega_m = 0.25$ , baryon density parameter  $\Omega_b = 0.045$ , Hubble constant  $h = 0.73$ , and the linear *RMS* density fluctuation in a sphere of an  $8 h^{-1}$ Mpc radius,  $\sigma_8 = 0.9$ . Note that this cosmology is different from the WMAP5 cosmology adopted here, but this should not be a problem as we use it only to test our method. The CDM density field of this simulation was traced by  $2160^3$  particles, each having a mass of  $M_p \sim 8.6 \times 10^8 h^{-1} M_\odot$ , in a cubic box of  $500 h^{-1}$ Mpc (comoving). The characteristic mass,  $M_*$ , defined to be the mass scale at which the *RMS* of the linear density field is equal to 1.686, is  $\log(M_*/h^{-1}M_\odot) \approx 12.8$ .

Dark matter halos were identified using the standard friends-of-friends algorithm (e.g. Davis et al. 1985) with a linking length that is 0.2 times the mean inter-particle separation. The mass of a halo,  $M_h$ , is simply defined as the sum of the masses of all the particles in the halo. These halos are referred to as ‘real halos’ in the following, to distinguish them from the groups identified by the group finder applied to the mock galaxy catalog described below.

Our construction of the mock galaxy and group catalogues here is similar to that described in Y07. First, we stack  $3 \times 3 \times 3$  replicates of the simulation box and populate the real haloes in the stacked boxes with galaxies of different luminosities, using the conditional luminosity function (CLF) model of van den Bosch et al. (2007). This CLF describes the halo occupation statistics of SDSS galaxies, and accurately matches the SDSS luminosity function and the clustering properties of SDSS galaxies as function of their luminosity. Phase-space parameters are assigned to the galaxies following the method described in More et al. (2009). Briefly, the brightest galaxy (central) in each halo is located at rest at the halo center, while the other galaxies (satellites) are distributed spherically following an NFW (Navarro, Frenk & White 1997) number density distribution with the concentration-mass relation of Macciò et al. (2007). At the assigned position of each satellite galaxy, one-dimensional velocities are drawn from a Gaussian with a dispersion computed from the Jeans equation assuming isotropy. Next we place a virtual observer at the center of the stacked boxes and assign each galaxy  $(\alpha_J, \delta_J)$  coordinates and a redshift, which is a combination of the galaxy's cosmological redshift and its peculiar velocity along the line-of-sight. Then we construct a mock galaxy catalogue by mimicking the sky coverage of the SDSS DR7, taking detailed account of the angular variations in the magnitude limits and completeness of the survey (see Li et al. 2007 for details). Finally, we apply the halo-based group finder of Yang et al. (2005) to the mock galaxy catalog to obtain a mock catalogue of groups with halo masses assigned according to their characteristic luminosities, as described in Y07 (see Section 2).

Similar to the SDSS group catalogue, the mock group catalogue is also complete to  $z \sim 0.12$  for groups with halo masses  $M_h \gtrsim 10^{12} h^{-1} M_\odot$ . We thus again adopt  $M_{\text{th}} = 10^{12} h^{-1} M_\odot$  and restrict our reconstruction to the volume covering the redshift range  $0.01 \leq z \leq 0.12$ . Note that this volume is called survey volume, and the survey volume for the mock catalogue is very similar to that of the real SDSS catalogue, so that the uncertainties in reconstruction arising from the survey boundaries are the same. The mock catalogue thus allows us to test the accuracy of the reconstruction from the real data. For the MS cosmology, Eq. (6) gives  $b_{\text{hm}} = 1.56$  for  $M_{\text{th}} = 10^{12} h^{-1} M_\odot$ , which is the value we will adopt for the mock catalogue.

## 4.2 Quantifying the SDSS Survey Volume

Because the structure outside the survey volume is not modelled accurately, the reconstruction is expected to be better in the inner region of the survey volume than near its boundary.

To quantify this boundary effect, we have to calculate the distance of each survey grid cell to the boundary. Unfortunately, the geometry of the survey volume is very complicated, and it is hard to calculate, or even define, the distance to the boundary. Hence we introduce a parameter, the filling factor  $F$ , to characterize the closeness of a survey grid cell to the boundary. For each survey grid cell,  $k$ , the filling factor  $F$  is defined as the fraction of grid cell centers in a spherical volume of radius  $R_F$  centered on  $k$ , that are located within the survey volume. Hence,  $F$  is expected to be much less than unity for a grid cell located close to the boundary, while  $F \simeq 1$  for a grid cell that is located more than a distance  $R_F$  from any survey boundary. Thus, the value of  $F$  can be used to quantify the closeness of a survey grid cell to the survey boundary. What remains is to specify the radius  $R_F$ . If  $R_F \rightarrow \infty$  then  $F \rightarrow 0$  for all  $k$ , while  $F \rightarrow 1$  for  $R_F \rightarrow 0$ . We adopt  $R_F = 80 h^{-1}\text{Mpc}$ , for which we obtain a useful dynamic range in values of  $F$ : for the SDSS DR7 survey volume, 25.4% of the survey grid cells have  $F \geq 0.9$ , 38.9% have  $F \geq 0.8$ , and 66.4% have  $F \geq 0.6$ . We note that our main results are insensitive to changes in  $R_F$  of a factor of two.

### 4.3 Testing the Reconstruction of the Velocity Field

The upper panels of Fig. 2 show the reconstructed velocity ( $\mathbf{v}_{\text{rec}}^{\text{m}}$ ) obtained from the mock catalogue using the method described in Section 3 versus the true velocity in the simulation ( $\mathbf{v}_{\text{sim}}$ ) (in contours), with smoothing mass scale  $\log(M_s/h^{-1}\text{M}_\odot) = 13$ . Here, we only plot the comparison of the  $Y$  component of the velocities, because its dynamic range is larger than in the other two directions and because the results for all the three directions are quite similar. Results are shown separately for grid cells with  $F \geq 0.9$ ,  $0.6 \leq F \leq 0.7$  and  $0.3 \leq F \leq 0.4$ , as indicated. For grid cells with  $F \geq 0.9$  (i.e. which are far from any survey boundary), the reconstructed velocity is tightly and linearly correlated with the true velocity (the upper-left panel). We have performed a linear regression and found a slope of 0.95. The best-fit line is shown in the figure as the dashed line. The value of the slope and the scatter around the best-fit relation are also given in the panel. As  $F$  decreases to  $\sim 0.65$ , the slope of the correlation (0.96) does not change significantly, but the tightness of the correlation decreases. Finally, for grid cells with  $F \sim 0.35$ , the best-fit slope of the correlation (0.62) deviates significantly from unity. Based on these results we conclude that our method can reliably reproduce the cosmic velocity field in regions with  $F \geq 0.6$ , which applies to about 66% of the SDSS survey volume, as mentioned above.

We then compare the results obtained above with those obtained with a larger smoothing mass scale,  $\log(M_s/h^{-1}\text{M}_\odot) = 14$ . As  $M_s$  increases, the correlation becomes tighter while the slope and the dynamic range of the velocity do not change significantly. The slopes of the correlation for grid cells within the three ranges of  $F$  are now 0.92, 0.91 and 0.59 respectively (see the lower panels of Fig. 2). This suggests that the velocity field is produced primarily by relatively large-scale structures. Indeed, for the CDM model considered here, the velocity field is dominated by structure on scales where the effective power index of the power spectrum is  $\sim -1$  [see Chapter 6 in Mo, van den Bosch & White (2010; hereafter MBW10)], which corresponds to a mass scale of  $\sim 10^{15} h^{-1}\text{M}_\odot$ .

Fig. 3 shows the probability distribution of the difference between the reconstructed and true velocities ( $v_{\text{rec}}^{\text{m}} - v_{\text{sim}}$ ). This confirms that the reconstruction is better for larger  $F$  and larger  $M_s$ . For  $F \geq 0.6$ , the distributions for the  $X$  and  $Y$  velocity-components peak nicely at zero, while for the  $Z$ -component the peaks are located at  $+50 \text{ km s}^{-1}$ , indicating a slight bias in the reconstruction. In fact, there is weak but systemic bias between  $v_{\text{rec}}^{\text{m}}$  and  $v_{\text{sim}}$  along all the three axes (see Fig. 2 and Fig. 4), in the sense that the absolute value of  $v_{\text{rec}}^{\text{m}}$  is, on average, smaller than that of  $v_{\text{sim}}$ . These systematic deviations can be caused by a number of factors. First of all, they may signal inaccuracies associated with the method itself. For example, the linear theory used to infer the velocity field from the gradient of the peculiar potential [Eq. (2)] is expected to be inaccurate for grid cells where nonlinear effects are not negligible. Secondly, the problem may arise from the fact that the survey volume is finite: velocity is generated by gravity, which is a long range force. Hence, if the survey volume is too small, the gravitational force due to the mass distribution outside the survey volume may make a significant contribution which is not included in our calculation. Thirdly, it may be that our correction for redshift distortions turns out to be inaccurate. And finally, systematic deviations in the reconstructed velocity field may also arise from inaccuracies (i.e., false identifications of groups) in our group finder.

In order to determine which, if any, of these factor(s) dominate, we perform a series of tests. For all these tests we keep the smoothing mass scale fixed at  $\log(M_s/h^{-1}\text{M}_\odot) = 13$ . For our first test we use real halos distributed in real space in the periodic simulation box ( $500 h^{-1}\text{Mpc}$ ) to predict the velocity ( $v_{\text{rec}}^{\text{b}}$ ) using linear theory. In this case, the reconstruction does not suffer from effects due to limited volume, redshift distortions or our group finder. Hence, a comparison between the reconstructed and true velocity fields in this case tests the accuracy of our method in the absence of ‘observational’ effects. The first column of

Fig. 4 shows the reconstructed velocity versus the true velocity along all three axes. The corresponding slope and scatter of the correlation are shown in each panel for comparison. As one can see, the correlations are steeper than a slope of unity and the deviation for all the three axes are similar, about 9%. This clearly shows that our method is not perfect, likely because of the use of linear theory in our model. To check the effects due to the limited survey volume, we use real halos distributed in real space, but only those located within the *survey volume*, to predict the velocity ( $v_{\text{rec}}^{\text{s}}$ ). The resulting correlation between  $v_{\text{rec}}^{\text{s}}$  and  $v_{\text{sim}}$  for survey grid cells with  $F \geq 0.6$  is shown in the second column of Fig. 4. The  $v_{\text{rec}}^{\text{s}} - v_{\text{sim}}$  correlations are flatter than the  $v_{\text{rec}}^{\text{b}} - v_{\text{sim}}$  correlations for all three velocity components. On average the slope decreases by about 7%, indicating that the large-scale structure outside the survey volume indeed contributes to the acceleration. Next we consider the effect due to redshift distortion. Using the velocities of real halos, we generate a halo sample in redshift space within the *survey volume*. We then use the method described in Section 3.1 to correct for the redshift distortion and apply our reconstruction method to estimate the velocity field ( $v_{\text{rec}}^{\text{z}}$ ). In this case, the correlation for cells with  $F \geq 0.6$  (shown in the third column) is similar to that between  $v_{\text{rec}}^{\text{s}}$  and  $v_{\text{sim}}$  (with an increase of 3% in the slope), suggesting that our method for correcting the redshift distortions works well and does not introduce significant bias. Finally, in the fourth column of Fig. 4 we show the correlation between  $v_{\text{rec}}^{\text{m}}$  and  $v_{\text{sim}}$  (again only for cells with  $F \geq 0.6$ ), which includes also the effect of our group finder. Here the correlation becomes flatter than the  $v_{\text{rec}}^{\text{z}} - v_{\text{sim}}$  correlation for all the three velocity components, albeit by a small amount (12% in the slope). This indicates that the group finder itself also introduces a weak bias.

The amplitudes of the deviation from a unity-slope relation introduced by the inaccuracy of the method (9%), the limited volume effect (−7%), and the group finder (−12%) are roughly comparable, and so all of them are important for producing the final deviation. Because this bias is relatively small and because it is extremely complicated to model accurately, we do not try to correct for it in what follows. Note that the scatter in the reconstructed velocity field (which is indicated in each panel) is mainly due to the inaccuracy of the method. We have also checked the distribution of the residual between the true velocity and each of the four reconstructed velocities. For the first case, where real halos distributed in real space in the periodic simulation box are used, the distributions of the three velocity components are identical. For the other three cases, where halos are distributed in the survey volume, the distributions are similar to those shown in Fig. 3 (see also Fig. 4). This suggests

that the differences between the three components in our mock tests are mainly due to the survey geometry.

#### 4.4 Testing the Reconstruction of the Tidal Field

We now move to the reconstruction of the cosmic tidal field. Fig. 5 shows the tidal field reconstructed from the mock catalogue,  $T_i^{\text{m}}(\text{rec})$ , versus the tidal field calculated directly from the MS simulation,  $T_i(\text{sim})$ , together with the best-fit linear relations and the corresponding values of the slope and the scatter. Fig. 6 shows the probability distribution of  $T_i^{\text{m}}(\text{rec}) - T_i(\text{sim})$  obtained for different choices of  $F$  and  $M_s$ . Overall, the eigenvalues of the reconstructed tidal tensor,  $T_i^{\text{m}}(\text{rec})$ , are strongly correlated with  $T_i(\text{sim})$ , albeit with a considerable bias and a large scatter for small  $M_s$ . The bias is almost absent and the scatter becomes much smaller as we adopt a larger smoothing scale,  $\log(M_s/h^{-1}\text{M}_\odot) = 14$ . Moreover the reconstruction is better for grid cells with larger  $F$ , similar to the velocity field. However, our results clearly show that the effect of  $F$  is not as important for the tidal field as for the velocity field. The reason is that the tidal field, being the derivative of the velocity field, is more dominated by smaller scale structure. This is also evident from the fact that the dynamic range of the reconstructed tidal field decreases significantly when  $\log(M_s/h^{-1}\text{M}_\odot)$  increases.

We have also carried out a series of tests to investigate what cause the scatter and bias in the tidal field reconstruction. As for the velocity field, we use the following four cases: (i) real halos in real space in the periodic simulation box; (ii) real halos in real space in the survey volume; (iii) real halos in redshift space and in the survey volume; and (iv) mock group catalogues. The reconstructed tidal fields are denoted by  $T_i^{\text{b}}(\text{rec})$ ,  $T_i^{\text{s}}(\text{rec})$ ,  $T_i^{\text{z}}(\text{rec})$  and  $T_i^{\text{m}}(\text{rec})$ , respectively. The comparisons of these reconstructions with the simulation results are shown in Fig. 7 for grid cells with  $F \geq 0.6$  (for the first test, the results for all grid cells are shown.). For all these tests we have adopted  $\log(M_s/h^{-1}\text{M}_\odot) = 13$ . Two things are worth noting. One is that the large scatter in the  $T_i^{\text{m}}(\text{rec})$ - $T_i(\text{sim})$  correlation is mainly caused by the inaccuracy of the method and the group finder, although other two effects also contribute to it. The other is that the deviation of the  $T_i^{\text{m}}(\text{rec})$ - $T_i(\text{sim})$  correlation from a slope of unity is inherited from the  $T_i^{\text{b}}(\text{rec})$ - $T_i(\text{sim})$  correlation, almost independent of the effects due to redshift distortion, limited volume and group finder. This deviation almost



disappears if we adopt  $\log(M_s/h^{-1}M_\odot) = 14$  (see Fig. 5), strongly suggesting that it is caused by non-linear effects on small scales.

## 5 APPLICATION TO THE SLOAN DIGITAL SKY SURVEY

So far we have demonstrated that our method is able to reliably reconstruct the velocity and tidal fields in regions with  $F \geq 0.6$ . In this section, we apply our method to the galaxy groups selected from the SDSS DR7. As noted in Section 2, we use groups with  $\log(M_h/h^{-1}M_\odot) \geq 12$  to perform the reconstruction in the survey volume ( $0.01 \leq z \leq 0.12$ ). For the WMAP5 cosmology and  $M_{\text{hm}} = 10^{12} h^{-1}M_\odot$  we obtain  $b_{\text{th}} = 1.69$  from Eq. (6), which is the value we adopted throughout. While we adopt a mass smoothing scale of  $\log(M_s/h^{-1}M_\odot) = 14.75$  for the correction for redshift distortions (as described in Section 3.1), the results presented below have been obtained using a smoothing mass scale of  $\log(M_s/h^{-1}M_\odot) = 13$ . Choosing the later scale to smooth our final results is a tradeoff between the accuracy and dynamic range.

### 5.1 The Tidal Field and the Classification of the Large-Scale Structure

Let us first look at the classification of the large-scale structure in the SDSS DR7 based on the reconstructed tidal tensor (see Section 3.2). Hahn et al. (2007a,b) found that using a smoothing mass scale of  $M_s = 2M_*$  yields good agreement with the visual classification of the large-scale structure. Since for the WMAP5 cosmology  $\log(M_*/h^{-1}M_\odot) \approx 12.5$ , our adopted smoothing scale of  $M_s = 10^{13} h^{-1}M_\odot$  nicely satisfies that criterion. Fig. 8 shows groups located in regions classified as **cluster** (red dots), **filament** (orange dots) and **sheet** (green dots) in a  $16 h^{-1}\text{Mpc}$  thick slice enclosing the SDSS Great Wall. Note that both groups with  $M_h \geq M_{\text{th}}$  and  $M_h < M_{\text{th}}$  are shown here. The orange dots nicely delineate the filamentary structure connecting the red dots, while green dots are more diffused, forming ‘envelops’ around the orange dots (lower-right panel). Such ‘hierarchical structure’ nicely accords with the CDM scenario of structure formation. Void groups are also shown, as blue dots in the lower-right panel, but since groups in voids are rare, it is difficult to use the distribution of groups to characterize a void region. We therefore show the grid cells in **void** in cyan in a plane with one cell thick centered at  $(-159, 90, 230)$  (in units of  $h^{-1}\text{Mpc}$ ), chosen to represent a large underdense region. The surrounding grid cells in **cluster**, **filament** and **sheet** are shown in red, orange and green respectively. For this particular region, the size

of the void is about  $100 h^{-1}\text{Mpc}$ . We also compute the volume filling fractions of the four different structures. The fractions in the  $F \geq 0.6$  region of the SDSS survey volume are about 1.9%, 31.8%, 53.2% and 13.1%, for **cluster**, **filament**, **sheet** and **void**, respectively, in good agreement with the results obtained from simulations (Hahn et al. 2007a; Forero-Romero et al. 2009) and from the SDSS galaxy redshift survey (Jasche et al. 2010).

## 5.2 The Velocity Field

Next let us look at the velocity fields in different regions. The arrows in Fig. 9 show the velocity vectors at the grid points, with their lengths proportional to their magnitudes. Note that the void region reveals a clearly divergent flow emerging from its center, and with a magnitude that increases with the distance from the center. The pattern is quite different in high density regions, such as the SDSS Great Wall shown in Fig. 10. Here the flow is clearly converging towards the central structure, and the velocity vectors have a tendency to be perpendicular to the filamentary structure. This behavior can be understood in terms of the Zel'dovich approximation (Zel'dovich 1970), which predicts that the velocity flow tends to be perpendicular to the largest dimensions of pancakes and filaments. To enhance the visual connection between the velocity field and the large scale structures, we also plot in these figures the distributions of both massive groups ( $M_h \geq M_{\text{th}}$ ; black dots) as well as low mass groups ( $M_h < M_{\text{th}}$ ; white dots) in slices  $4 h^{-1}\text{Mpc}$  thick, and also show the **cluster**, **filament**, **sheet** and **void** regions in red, orange, green and cyan, respectively.

Convergent flow are also predicted to be present around smaller filamentary structures. We select a relatively small structure ( $38 h^{-1}\text{Mpc} \times 34 h^{-1}\text{Mpc}$  comoving) and show its surrounding velocity field in the left panel of Fig. 11, using the same color coding as in Fig. 10. This small structure has apparent bulk motions towards negative  $Y$  direction, which may be induced by nearby massive structures and dominate over the peculiar velocities produced by the more local mass distribution. However, we still can see the signal of convergent flow. To demonstrate this more clearly, we show the velocity field *relative to the velocity of its center of mass* in the right panel. The velocity flow clearly converges towards and is perpendicular to the small filament. Interestingly, the flow seems to converge predominantly towards the low mass groups with  $M_h < M_{\text{th}}$  (white dots), which are not used in our derivation of the velocity or tidal fields. This suggests that the large scale tidal field can compress masses into filamentary/sheet-like structures, in accord with the Zel'dovich approximation (Zel'dovich

1970). Note that the results shown in Fig. 8, 9, 10 and 11 are not restricted to  $F \geq 0.6$  regions, although most of the regions in the first three figures, and all of the regions in the last figure, have  $F \geq 0.6$ .

Finally, in Fig. 12 we show the probability distribution of the three velocity components ( $v_x$ ,  $v_y$  and  $v_z$ ) for grid cells with  $F \geq 0.6$ . As before, we have adopted a smoothing mass scale of  $\log(M_s/h^{-1}M_\odot) = 13$ . Using  $\log(M_s/h^{-1}M_\odot) = 14$  or 15 gives quite similar results, although the dynamic range decreases slightly as  $\log(M_s/h^{-1}M_\odot)$  increases. The distribution of each velocity component is approximately Gaussian with extended wings, consistent with the finding of Sheth & Diaferio (2001). The best-fitting Gaussian profiles for both the  $X$  and  $Y$  components peak roughly at zero, with a dispersion of about  $360 \text{ km s}^{-1}$ , again in good agreement with the prediction of the current  $\Lambda$ CDM model (Sheth & Diaferio 2001). However, the Gaussian profile for the  $Z$ -component peaks at about  $-117 \text{ km s}^{-1}$  and has dispersion of  $413 \text{ km s}^{-1}$ . This suggests that a bulk flow is present over a volume about 66% of the survey volume (where  $F \geq 0.6$ ), which is equivalent to a sphere with a radius of  $\sim 170 h^{-1} \text{ Mpc}$ . Such a bulk flow implies the existence of one or more massive structures at small  $Z$  (i.e. small  $\delta_J$ ) in the survey volume. Such a large-scale inhomogeneity is indeed present, in the form of the SDSS Great Wall, which is located near  $\delta_J = 4^\circ$ , with a redshift of 0.08 (Gott et al. 2005; see also Fig. 1). It would be interesting to investigate such large-scale flows further in comparison with those given by other methods, such as measurements based on distance indicators (e.g. Watkins et al. 2009; Feldman et al. 2010).

### 5.3 A New Method to Reconstruct the Density Field

As described in Section 1, W09 presented a new method to reconstruct the matter density field from the distribution of (relatively) massive groups (i.e., dark matter haloes). The method partitions the volume in domains associated with each individual group, and models the mass distribution in each domain using the cross-correlation function between dark matter haloes and the mass distribution within their domain obtained from  $N$ -body simulations. Here we present an alternative method to reconstruct the density field, which is significantly less elaborate in that it does not require  $N$ -body simulations to characterize the halo-matter cross-correlation in halo domains.

Rather, our new method uses the Zel'dovich (1970) approximation to displace mass elements using the velocity field obtained using the method described in Section 3 (see also

Nusser et al. 1991). According to the Zel’dovich approximation, the growth of structure can be specified by the displacement of mass elements from their initial positions, and the displacement,  $\mathbf{r} - \mathbf{r}_i$ , of each mass element is proportional to the gradient of the *initial* gravitational potential at the initial position,  $\mathbf{r}_i$ . Since the potential  $\phi \propto D(a)/a$  and  $\mathbf{v} \propto \nabla\phi$  [equation (2)], we can also use the velocity field at redshift zero, instead of the initial potential, to calculate the displacement:

$$\mathbf{r} = \mathbf{r}_i + \frac{\mathbf{v}_0(\mathbf{r}_i)}{H_0 a_0 f(\Omega_0)} \frac{D(a)}{D(a_0)}, \quad (12)$$

[see § 4.1.8 of MBW10] where  $\mathbf{v}_0(\mathbf{r}_i)$  is the velocity vector at redshift zero at the initial position of the mass element. Since the initial density perturbations are small, one may use particles located on a uniform grid to sample the initial density field. The above equation can then be used to predict the positions of the particles at  $a = 1$  ( $z = 0$ ) (or at any other redshift), thereby obtaining the density field.

Here we apply Eq. (12) to our reconstructed velocity field for the SDSS DR7 survey volume to predict the corresponding large-scale density field. We start by generating a sample of  $512^3$  particles uniformly distributed in the survey box, which we subsequently displace using the reconstructed velocity field. The resulting density field at redshift of zero, smoothed with a Gaussian kernel with a mass scale of  $\log(M_s/h^{-1}M_\odot) = 13$ , is shown in the bottom panel of Fig. 13. Comparing this reconstructed density field with the group distribution shown in Fig. 8, one can see clearly the mass concentrations associated with massive structures, such as the SDSS Great Wall. Furthermore, one can also see smaller filaments that are not so evidently seen in the group distribution itself. For comparison, we also show the predicted density fields at  $z = 2$  (middle panel) and  $z = 4$  (top panel). A comparison among the different panels nicely illustrates the hierarchical formation of the SDSS Great Wall.

Since this paper focusses on the velocity and tidal fields reconstructed from the SDSS DR7, we refrain from a detailed quantification of the accuracy of this reconstruction method. A detailed test of this method against  $N$ -body simulations, as well as an in-depth comparison with the reconstruction method proposed in W09, will be presented in a forthcoming paper. For the moment we only emphasize that the new method presented here, albeit simpler and less time-consuming, is unable, by construction, to resolve highly non-linear structures. Hence, unlike the W09 method, it is only able to reconstruct density field smoothed on relatively large scales. Its advantage, however, is that it automatically yields the reconstructed

density field *as a function of time*, therefore providing insight into the merger/assembly history of the large-scale structure that hosts the galaxies in the SDSS DR7.

## 6 DISCUSSION AND SUMMARY

W09 have developed a method to reconstruct the velocity and tidal fields from the distribution of dark matter haloes. In this paper, we use the method to reconstruct these two fields in the Sloan Digital Sky Survey (SDSS) DR7 volume from dark matter halos represented by galaxy groups. We use detailed mock catalogues to test the reliability of our method against uncertainties arising from the inaccuracies of our method, redshift distortions, survey boundaries and false identifications of groups by our group finder. We find that both the velocity and tidal fields can be reliably reconstructed in the inner region of the survey volume, but that the reconstruction near the survey boundaries is significantly biased, especially the velocity field, which is more sensitive to large scale structure. We define a quantity to quantify the closeness to the survey boundary, and find that for the SDSS DR7 the bias produced by the boundary effects becomes comparable to or smaller than that produced by other factors for the inner  $\sim 66\%$  of the survey volume. The total bias in the reconstruction quantities is small, and detailed analysis suggest that each of the factors mentioned above contributes roughly equally to the bias. These results show that our method can be applied to real data to get reliable results.

We apply our method to the galaxy group catalogue obtained from the SDSS DR7 using the halo-based group finder of Yang et al. (2005). We use the reconstructed tidal field to classify the morphologies of large scale structures, based on the number of positive eigenvalues of the tidal tensor. This reveals clearly a cosmic web, with filamentary structures connecting clusters and enveloped by sheet-like structures that surround large voids. In particular, the volume filling fractions of the four structures are in good agreement with the simulations. As examples, we show the velocity fields in the region of a large void, a large region covering the SDSS Great Wall, and in the neighborhood of a small filament. In agreement with expectations, the velocity fields are clearly divergent in the centers of voids, while converging towards sheets (along one direction), filaments (along two directions) and clusters (along all three directions). The distribution of the resulting velocities has an approximate Gaussian core with extended wings, consistent with model expectations. The Gaussian cores for both the  $X$  and  $Y$  components peak roughly at zero, with a dispersion of about  $360 \text{ km s}^{-1}$ , in

good agreement with prediction for the  $\Lambda$ CDM concordance cosmology. However, the distribution of the  $Z$  component peaks at about  $-117 \text{ km s}^{-1}$  and has a larger dispersion of  $413 \text{ km s}^{-1}$ . This suggests that a large fraction of the entire SDSS survey volume (equivalent to a sphere with a radius of  $\sim 170 h^{-1} \text{ Mpc}$ ) is undergoing a bulk flow of  $\sim 120 \text{ km s}^{-1}$ . Based on the direction of this bulk flow, it is most likely due to the gravitational attraction from massive structures, including the SDSS Great Wall, located at low declination.

We have also used the reconstructed velocity field, together with the Zel'dovich approximation, to reconstruct the cosmic density field in the SDSS survey volume. Visual inspections show that this method can well reproduce both the massive structures populated by rich groups, and small structures populated by individual galaxies. However, since it is based on the Zel'dovich approximation, it is unable to resolve highly non-linear regions, unlike the method presented in W09, which is based on an analog of the ‘halo model’ (e.g., Cooray & Sheth 2002) that describes the matter density distribution (in a statistical sense) in terms of its halo building blocks. Nevertheless this reconstruction has the advantage of being able to trace the density field across cosmic times, thus providing insight into the assembly of the large scale structure that hosts the SDSS galaxies.

The reconstructed velocity, tidal and density fields presented here have many applications. For instance, together with the SDSS DR7 group catalogue, our reconstructed cosmic fields can be used to investigate how galaxy properties correlate with their environment. In particular, it would be interesting to investigate whether galaxies in a halo of given mass  $M$  that is located in a filament differ, in a statistical sense, from galaxies in haloes of the same mass but located in a void, cluster or sheet. Recent studies have suggested that the properties of dark matter halos do depend significantly on their large-scale environments (e.g. Lee & Pen 2001; Gao et al. 2005; Wechsler et al. 2006; Jing et al. 2007; Wang et al. 2007, 2011), and it remains to be seen whether this is also the case for galaxies. The reconstructed density, velocity and tidal fields presented here, together with the intrinsic properties observed for SDSS galaxies, will provide a unique and novel avenue to study how environmental effects affect the properties of galaxies.

The fact that our reconstructed velocity field, together with the Zel'dovich approximation, seems able to yield a reliable density field on large, quasi-linear scales also indicates that it can be used to set up the initial conditions for  $N$ -body simulations of the large-scale structure formation in the local universe. In practice, the velocity field has to be smoothed on a suitable scale such that strongly nonlinear structures are absent and the Zel'dovich

approximation is valid. The missing part of the perturbation spectrum in the initial conditions on small scales can be included using the method developed by, e.g., Bertschinger (1987), Hoffman & Ribak (1992), and van de Weygaert & Bertschinger (1996). These initial conditions can then be used to run constrained simulations that closely mimic the true large scale structure in the SDSS survey volume (see also e.g. Nusser & Dekel 1992; Kolatt et al. 1996; Klypin et al. 2003; Kitauro & Ensslin 2008; Forero-Romero et al. 2011). Our reconstructed density field based on the Zel'dovich approximation demonstrates the potential of this method, but further investigation along this line is needed. The hope is that eventually the formation history of the local universe can be traced back in time with reasonable accuracy. A comparison with the observed galaxy population within the same volume will then provide a goldmine to explore how galaxies form and evolve.

The reconstructed density and velocity fields will also be useful for studying the dynamics and physics of the IGM. For example, the line-of-sight peculiar velocities of the most massive groups in the SDSS DR7 survey volume can be used to make detailed predictions for the kinetic Sunyaev-Zel'dovich effect, which can be compared to forthcoming observations from, e.g., the Atacama Cosmology Telescope (ACT; Swetz et al. 2011) and the Planck satellite. In addition, a comparison of the reconstructed density field with quasar absorption line studies that are sensitive to the absorptions in the SDSS DR7 survey volume can provide invaluable constraints on the temperature and metallicity of the filaments and sheets that make up the cosmic web. Observations have so far revealed a wide array of absorption lines, ranging from low ions such as HI all the way up to highly ionized species, such as OVI and NeVIII (Tripp & Bowen 2006 and references therein), presumably associated with the warm-hot medium seen in gas-dynamical simulations (e.g. Cen & Ostriker 1999; Davé et al. 2001). With the installation of the *Cosmic Origins Spectrograph* (COS) on the *HST*, the sample of UV absorption systems in the local universe should increase by an order-of-magnitude or more. Such observations, together with the information about the density and velocity fields obtained from our reconstruction, provide an unique avenue to understand the nature of absorption systems at low- $z$  and their implications for the state and structure of the IGM at the present time, and in particular to explore the connection and interaction between the IGM and the galaxy population.

Our reconstructed velocity field can also be used to constrain cosmological parameters via a comparison with the peculiar velocity field obtained from distance indicators (e.g. Kaiser et al. 1991; Willick & Strauss 1998; Hudson et al. 2004; Colombi et al. 2007). It should be kept

in mind that our reconstruction method is cosmology dependent: cosmology enters through the method we use to assign halo masses to our galaxy groups (see Y07 for details), and via the bias parameter,  $b_{\text{hm}}$  (Eq. [6]) and the cosmological parameters  $\Omega_{\text{m}}$  and  $H_0$  that enter the reconstruction of the velocity field. Since methods that rely on distance indicators are less cosmology-dependent, a comparison of the velocity fields obtained using both methods may be able to constrain one or more cosmological parameters. Previous studies usually used the galaxy distribution directly to compare to the velocity field. However, galaxies are known to be biased tracers of the large scale mass distribution and the exact form of this bias is complicated, as it depends on various properties of the galaxies, such as luminosity and color. Thus using galaxies directly may introduce uncertainties into the estimate of cosmological parameters. Our reconstructed velocity field is a better choice for this purpose, because the bias of dark matter halos is well understood. In particular, it is interesting to investigate if the large-scale bulk flow revealed in our analysis might pose a challenge to the standard  $\Lambda$ CDM model.

The reconstructed density, velocity and tidal fields presented here are publicly available from the authors upon request. We hope that they will provide a useful piece of data for investigations in cosmology, large-scale structure, galaxy formation, and the IGM.

## ACKNOWLEDGMENTS

This work is supported by NSFC (11073017, 10821302, 10925314, 11128306), 973 program (2007CB815402, 2009CB824800) and the Fundamental Research Funds for the Central Universities. HJM would like to acknowledge the support of NSF AST-0908334 and the CAS/SAFEA International Partnership Program for Creative Research Teams (KJ CX2-YW-T23).

## REFERENCES

- Abazajian K. N., et al., 2009, *ApJS*, 182, 543
- Adelman-McCarthy J. K., et al., 2006, *ApJS*, 162, 38
- Aragón-Calvo M. A., Jones B. J. T., van de Weygaert R., van der Hulst J. M., 2007, *A&A*, 474, 315
- Aragón-Calvo M. A., van de Weygaert R., Jones B. J. T., 2010a, *MNRAS*, 408, 2163
- Aragón-Calvo M. A., Platen E., van de Weygaert R., Szalay A. S., 2010b, *ApJ*, 723, 364



- Bell E. F., McIntosh D. H., Katz N., Weinberg M. D., 2003, *ApJS*, 149, 289
- Bertschinger E., 1987, *ApJ*, 323, 103
- Blanton M. R., et al., 2005, *AJ*, 129, 2562
- Bond J. R., Kofman L., Pogosyan D., 1996, *Natur*, 380, 603
- Cen R., Ostriker J. P., 1999, *ApJ*, 514, 1
- Colombi S., Chodorowski M. J., Teyssier R., 2007, *MNRAS*, 375, 348
- Cooray A., Sheth R., 2002, *Phys. Rep.* 372, 1
- Davé R., et al., 2001, *ApJ*, 552, 473
- Davis M., Efstathiou G., Frenk C. S., White S. D. M., 1985, *ApJ*, 292, 371
- Dunkley J., et al., 2009, *ApJS*, 180, 306
- Erdoğan P., et al., 2004, *MNRAS*, 352, 939
- Feldman H. A., Watkins R., Hudson M. J., 2010, *MNRAS*, 407, 2328
- Fisher K. B., Lahav O., Hoffman Y., Lynden-Bell D., Zaroubi S., 1995, *MNRAS*, 272, 885
- Forero-Romero J. E., Hoffman Y., Gottlöber S., Klypin A., Yepes G., 2009, *MNRAS*, 396, 1815
- Forero-Romero J. E., Hoffman Y., Yepes G., Gottlöber S., Piontek R., Klypin A., Steinmetz M., 2011, *MNRAS*, 417, 1434
- Gao L., Springel V., White S. D. M., 2005, *MNRAS*, 363, L66
- Gott J. R., III, Jurić M., Schlegel D., Hoyle F., Vogeley M., Tegmark M., Bahcall N., Brinkmann J., 2005, *ApJ*, 624, 463
- Hahn O., Carollo C. M., Porciani C., Dekel A., 2007b, *MNRAS*, 381, 41
- Hahn O., Porciani C., Carollo C. M., Dekel A., 2007a, *MNRAS*, 375, 489
- Hoffman Y., Ribak E., 1992, *ApJ*, 384, 448
- Hoyle F., Vogeley M. S., 2002, *ApJ*, 566, 641
- Hudson M. J., Smith R. J., Lucey J. R., Branchini E., 2004, *MNRAS*, 352, 61
- Jasche J., Kitaura F. S., 2010, *MNRAS*, 407, 29
- Jasche J., Kitaura F. S., Li C., Enßlin T. A., 2010, *MNRAS*, 409, 355
- Jing Y. P., 1998, *ApJ*, 503, L9
- Jing Y. P., Suto Y., Mo H. J., 2007, *ApJ*, 657, 664
- Kang X., Jing Y. P., Mo H. J., Börner G., 2005, *ApJ*, 631, 21
- Kaiser N., Efstathiou G., Saunders W., Ellis R., Frenk C., Lawrence A., Rowan-Robinson M., 1991, *MNRAS*, 252, 1
- Kitaura F. S., Enßlin T. A., 2008, *MNRAS*, 389, 497

- Kitaura F.-S., Jasche J., Metcalf R. B., 2010, MNRAS, 403, 589
- Klypin A., Hoffman Y., Kravtsov A. V., Gottlöber S., 2003, ApJ, 596, 19
- Kolatt T., Dekel A., Ganon G., Willick J. A., 1996, ApJ, 458, 419
- Lahav O., Lilje P. B., Primack J. R., Rees M. J., 1991, MNRAS, 251, 128
- Lee J., Pen U-L., 2001, ApJ, 555, 106
- Li C., Jing Y. P., Kauffmann G., Börner G., Kang X., Wang L., 2007, MNRAS, 376, 984
- Macciò A. V., Dutton A. A., van den Bosch F. C., Moore B., Potter D., Stadel J., 2007, MNRAS, 378, 55
- Mo H. J., White S. D. M., 1996, MNRAS, 282, 347
- Mo H. J., van den Bosch F. C., White S. D. M., 2010, Galaxy Formation and Evolution, Cambridge University Press (MBW10)
- More S., van den Bosch F. C., Cacciato M., Mo H. J., Yang X., Li R., 2009, MNRAS, 392, 801
- Munoz-Cuartas J. C., Mueller V., Forero-Romero J., 2011, arXiv1107.1062
- Navarro J. F., Frenk C. S., White S. D. M., 1997, ApJ, 490, 493
- Nusser A., Dekel A., 1992, ApJ, 391, 443
- Nusser A., Dekel A., Bertschinger E., Blumenthal G. R., 1991, ApJ, 379, 6
- Park C., et al., 2005, ApJ, 633, 11
- Pillepich A., Porciani C., Hahn O., 2010, MNRAS, 402, 191
- Reed D. S., Bower R., Frenk C. S., Jenkins A., Theuns T., 2009, MNRAS, 394, 624
- Romano-Díaz E., van de Weygaert R., 2007, MNRAS, 382, 2
- Seljak U., Warren M. S., 2004, MNRAS, 355, 129
- Sheth R. K., Diaferio A., 2001, MNRAS, 322, 901
- Sheth R. K., Mo H. J., Tormen G., 2001, MNRAS, 323, 1
- Sheth R. K., Tormen G., 1999, MNRAS, 308, 119
- Sousbie T., Pichon C., Kawahara H., 2011, MNRAS, 414, 384
- Springel V., et al., 2005, Natur, 435, 629
- Swetz D. S., et al., 2011, ApJS, 194, 41
- Tinker J. L., Robertson B. E., Kravtsov A. V., Klypin A., Warren M. S., Yepes G., Gottlöber S., 2010, ApJ, 724, 878
- Tripp T., Bowen D. V., 2006, in P. Williams et al. eds. Probing galaxies through quasar absorption lines, IAU Colloquium 199, Cambridge Univ. Press. P5
- van den Bosch F. C., et al., 2007, MNRAS, 376, 841

- van de Weygaert R., Bertschinger E., 1996, MNRAS, 281, 84
- Wang H. Y., Mo H. J., Jing Y. P., 2007, MNRAS, 375, 633
- Wang Y., Yang X., Mo H. J., van den Bosch F. C., Weinmann S. M., Chu Y., 2008, MNRAS, 687, 919
- Wang H., Mo H. J., Jing Y. P., Guo Y., van den Bosch F. C., Yang X., 2009, MNRAS, 394, 398 (W09)
- Wang H., Mo H. J., Jing Y. P., Yang X., Wang Y., 2011, MNRAS, 413, 1973
- Watkins R., Feldman H. A., Hudson M. J., 2009, MNRAS, 392, 743
- Wechsler R. H., Zentner A. R., Bullock J. S., Kravtsov A. V., Allgood B., 2006, ApJ, 652, 71
- Weinmann S. M., van den Bosch F. C., Yang X., Mo, H. J., 2006, MNRAS, 366, 2
- White S. D. M., 1984, ApJ, 286, 38
- Willick J. A., Strauss M. A., 1998, ApJ, 507, 64
- Yang X., Mo H. J., van den Bosch F. C., 2003, MNRAS, 339, 1057
- Yang X., Mo H. J., van den Bosch F. C., Jing Y. P., 2005, MNRAS, 356, 1293
- Yang X., Mo H. J., van den Bosch F. C., Pasquali A., Li C., Barden M., 2007, ApJ, 671, 153
- York D. G., et al., 2000, AJ, 120, 1579
- Zaroubi S., Hoffman Y., Fisher K. B., Lahav O., 1995, ApJ, 449, 446
- Zel'Dovich Y. B., 1970, A&A, 5, 84

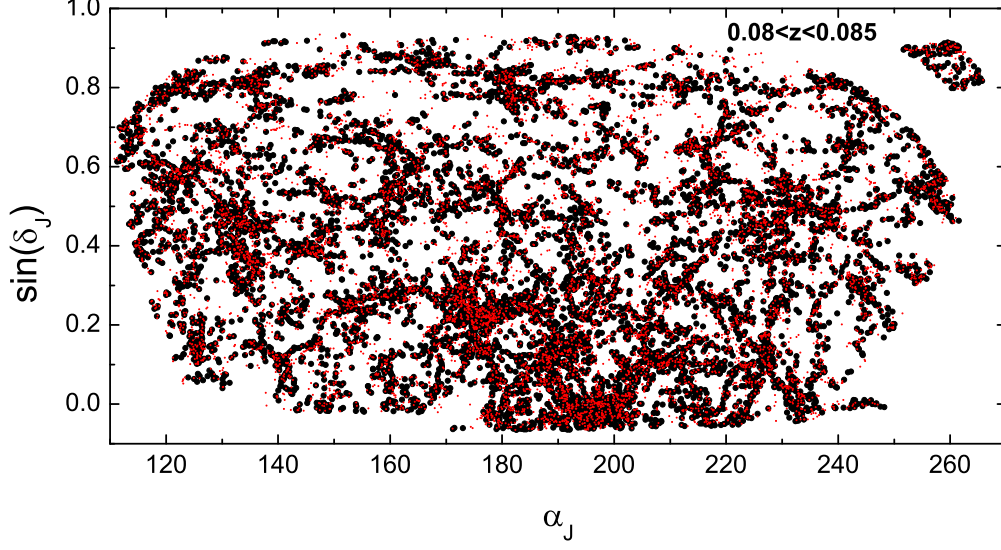


**Figure 1.** The distribution of the SDSS groups with  $\log(M_h / h^{-1} M_\odot) \geq 12$  (black dots), in comparison to the distribution of galaxies that are assigned to halos with smaller masses (red dots), in a specific redshift slice of  $0.08 \leq z \leq 0.085$ .

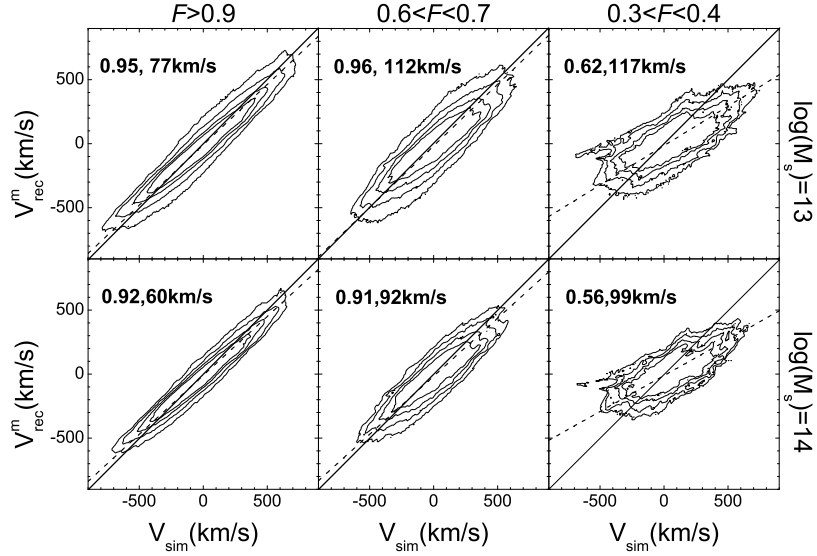


**Figure 2.** The Y-component of the predicted velocity based on the mock group catalogue versus the corresponding velocity obtained from the simulation. Results are shown for grid cells within three different ranges of filling factors,  $F$  (see text for definition), and with two smoothing mass scales as indicated in the figure. The four contours in each panel encompass 67%, 80%, 90% and 95% of the grid cells in a given range of  $F$ . The velocity field and tidal field shown below are obtained based on groups with  $M_{\text{th}} = 10^{12} h^{-1} M_\odot$ . The solid lines indicate the unity slope relationship, while the dashed lines show the best-fit linear relation of the correlation between the reconstruction and the simulation. The first number in each panel is the slope of the best-fit relation and the second number indicates the scatter around the best-fit line.

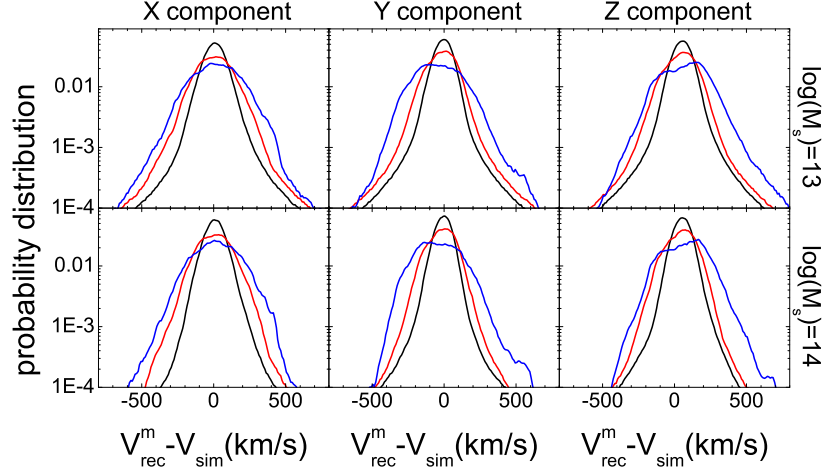


**Figure 3.** The probability distribution of the difference between the predicted and real velocities along  $X$ ,  $Y$  and  $Z$  axes (left, middle and right panels respectively). Results are shown for two choices of smoothing mass scales, as indicated. The black, red and blue lines in each panel show the results for grid cells with  $F \geq 0.9$ ,  $0.6 \leq F \leq 0.7$  and  $0.3 \leq F \leq 0.4$ , respectively.

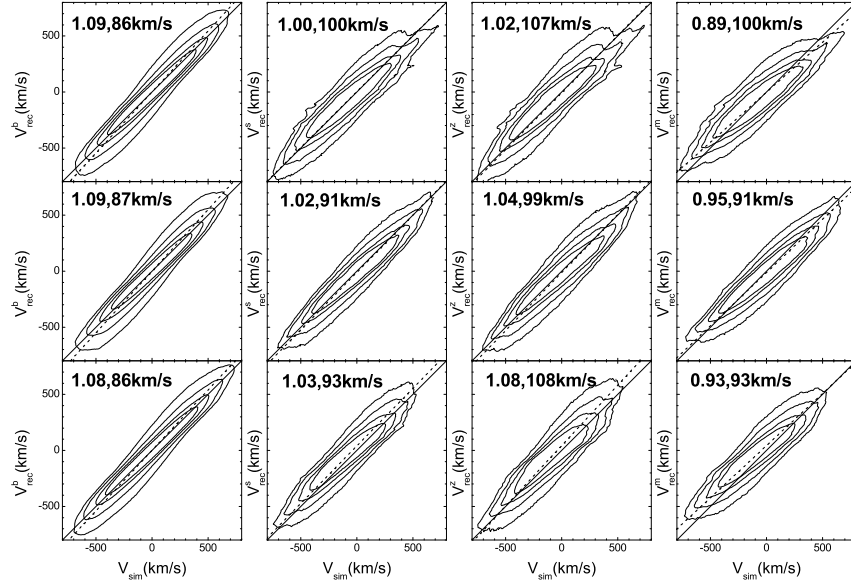


**Figure 4.** The predicted versus simulation velocities based on different group catalogues. The top, middle and bottom panels show the results along  $X$ ,  $Y$  and  $Z$  axes, respectively. The four contours in each panel encompass 67%, 80%, 90% and 95% of the grids. Results are only shown for  $\log(M_s/h^{-1}M_\odot) = 13$ . The first column panels show the predicted velocity based on real halos distributed in real space and in the periodic simulation box. The second column panels show the results based on real halos distributed in redshift space and in the survey volume. The third column panels show the results based on real halos distributed in redshift space and in the survey volume. The fourth column panels show the results based on the mock group catalogue. Note that redshift distortion is corrected for the last two cases. The dashed lines are the best linear fit, and the numbers are the slopes of these best fit relation and the scatter of the correlation relative to the best fit.

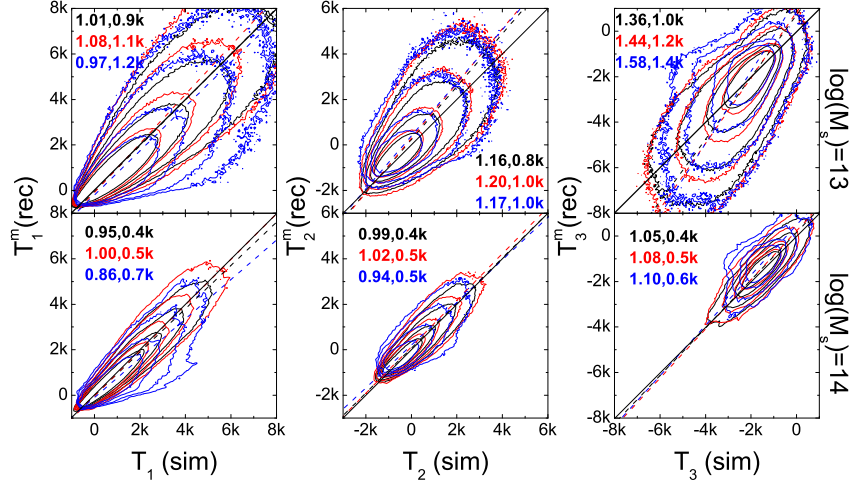


**Figure 5.** The three eigenvalues of the predicted tidal tensor from the mock group catalogue versus these obtained from the simulation. Results are shown for two choices of the smoothing mass scale, as indicated. Results for grid cells with  $F \geq 0.9$ ,  $0.6 \leq F \leq 0.7$  and  $0.3 \leq F \leq 0.4$  are shown in black, red and blue, respectively. The four contours for each result encompass 67%, 80%, 90% and 95% of the grid cells, respectively. The dashed lines are the best-fit, and the numbers are the slopes of the best-fit and the scatter relative to the best fit.

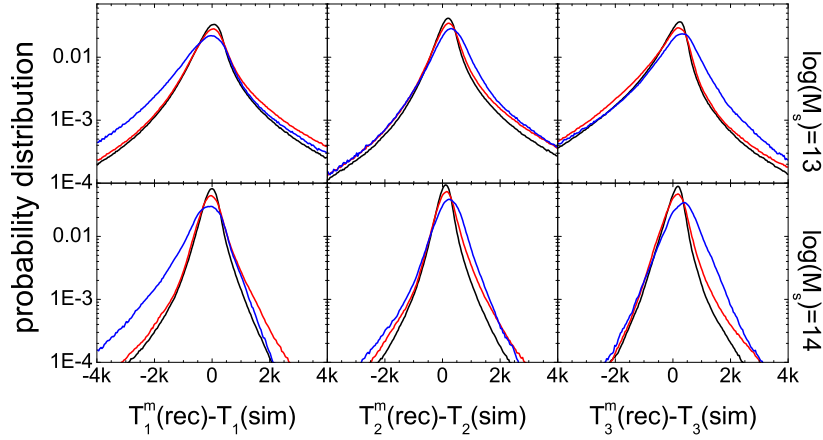


**Figure 6.** The probability distribution of the difference between the predicted eigenvalues of the tidal tensor and the eigenvalues obtained from simulation. The results with two smoothing mass scales are shown, as indicated. The black, red and blue lines in each panel show the results for grid cells with  $F \geq 0.9$ ,  $0.6 \leq F \leq 0.7$  and  $0.3 \leq F \leq 0.4$ , respectively.

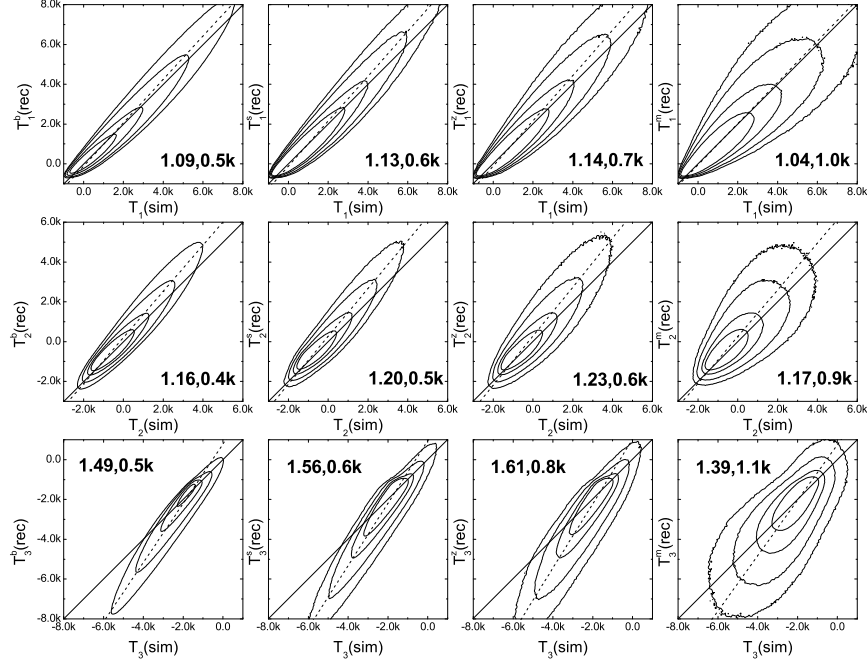


**Figure 7.** The same as Fig. 4 but for the eigenvalues of the tidal tensor.

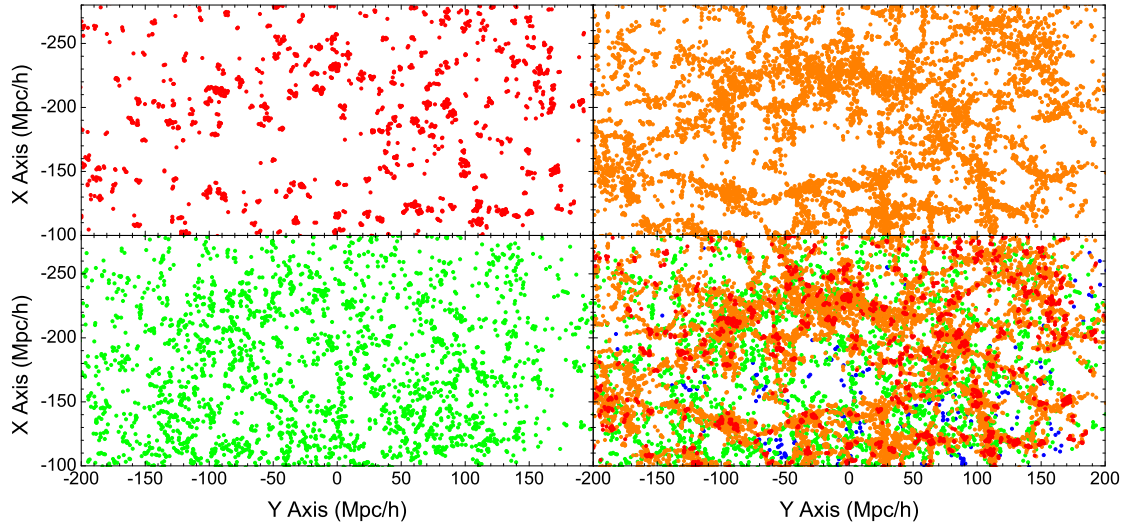


**Figure 8.** Classification of the large scale structure in a slice  $16 h^{-1} \text{Mpc}$  thick enclosing the SDSS Great Wall. The red dots are groups located at points classified as cluster. The orange dots are the groups located at points classified as filament. The green dots are groups located at sheet points, while the blue dots in the lower right panel are groups located at void points. Both groups with masses  $M_h \geq M_{\text{th}}$  and  $M_h < M_{\text{th}}$  are shown. Positions of these groups are corrected for redshift distortion.

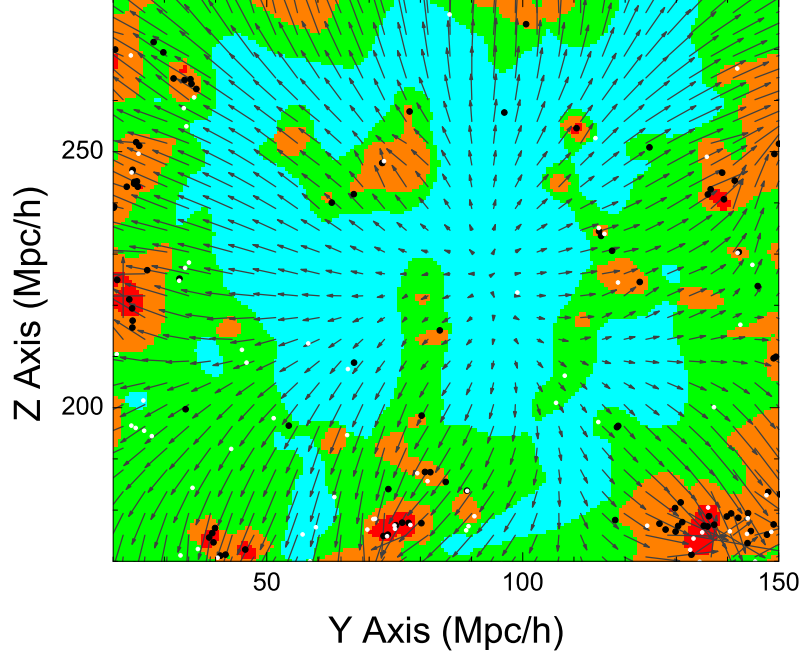


**Figure 9.** The velocity field in the  $Y - Z$  plane with  $X = -159 h^{-1} \text{Mpc}$  (grey vectors), together with the distribution of groups (dots) in a slice  $4 h^{-1} \text{Mpc}$  thick. The black dots are groups with masses larger than  $10^{12} h^{-1} \text{M}_{\odot}$ , while the white dots are the rest of the groups. Positions of the groups are corrected for redshift distortion. The grid cells in cluster, filament, sheet and void are show in red, orange, green and cyan, respectively.

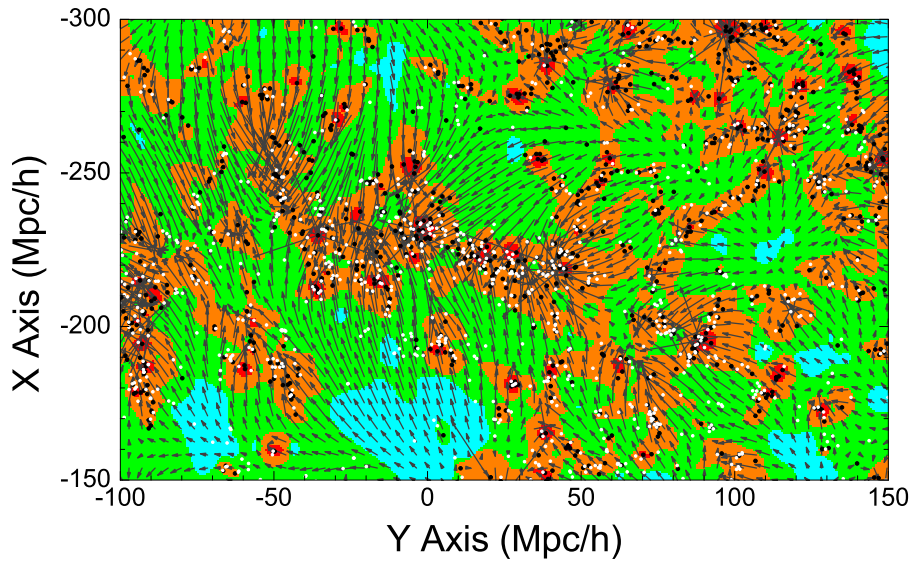


**Figure 10.** The velocity field in the  $Y - X$  plane with  $Z = 8 h^{-1} \text{Mpc}$  (gray vectors), together with the distribution of groups (dots) in a slice  $4 h^{-1} \text{Mpc}$  thick. The symbols and color coding are the same as in Fig. 9. Positions of the groups are corrected for redshift distortion. Note that the massive structure shown here is part of the SDSS Great Wall.



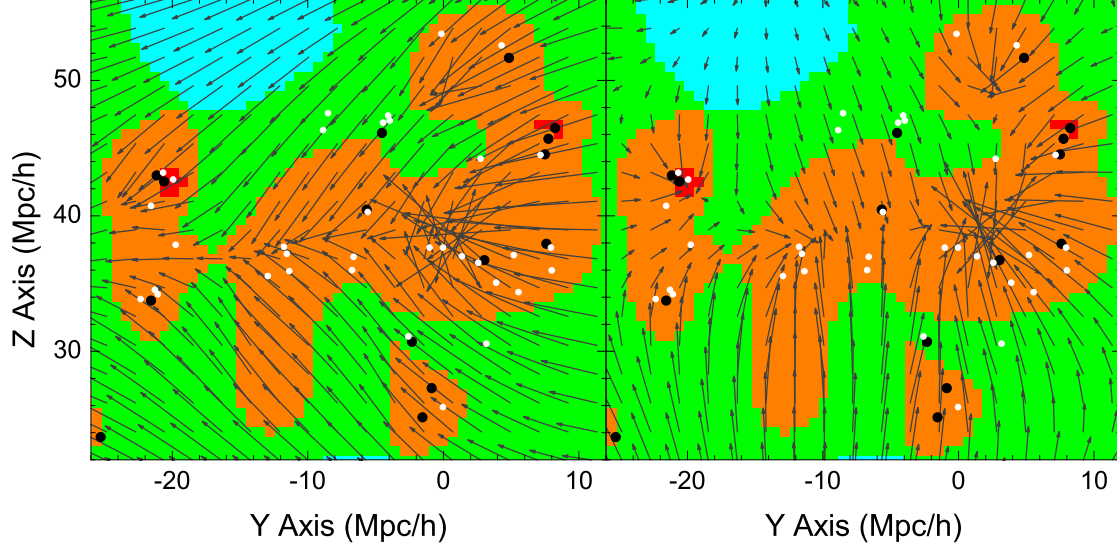


**Figure 11.** The velocity field (left panel) and the velocity field relative to the center of mass velocity (right panel) of a small structure in the  $Y$ - $Z$  plane with  $X = -159 h^{-1} \text{Mpc}$  (gray vectors), together with the distribution of groups (dots) in a slice  $4 h^{-1} \text{Mpc}$  thick. Positions of the groups are corrected for redshift distortion. The symbols and color coding are the same as in Fig. 9.

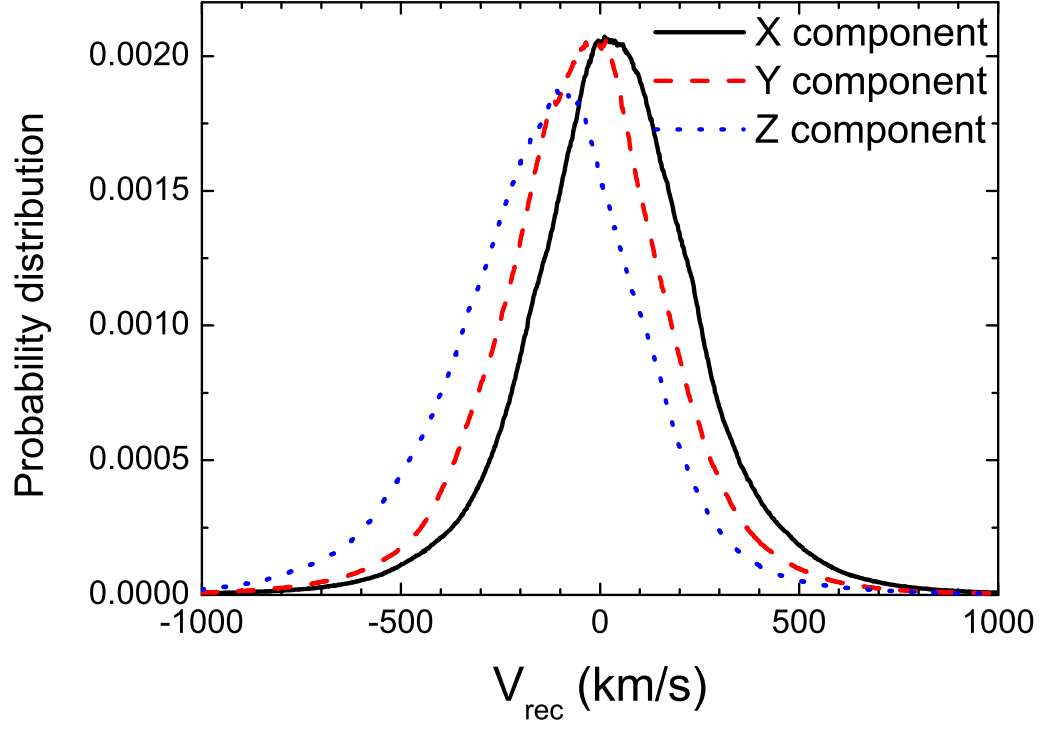


**Figure 12.** The probability distributions of the predicted velocities on grid cells with  $F \geq 0.6$  in  $X$ ,  $Y$  and  $Z$  directions. The smoothing mass scale is  $10^{13} h^{-1} \text{M}_{\odot}$ .

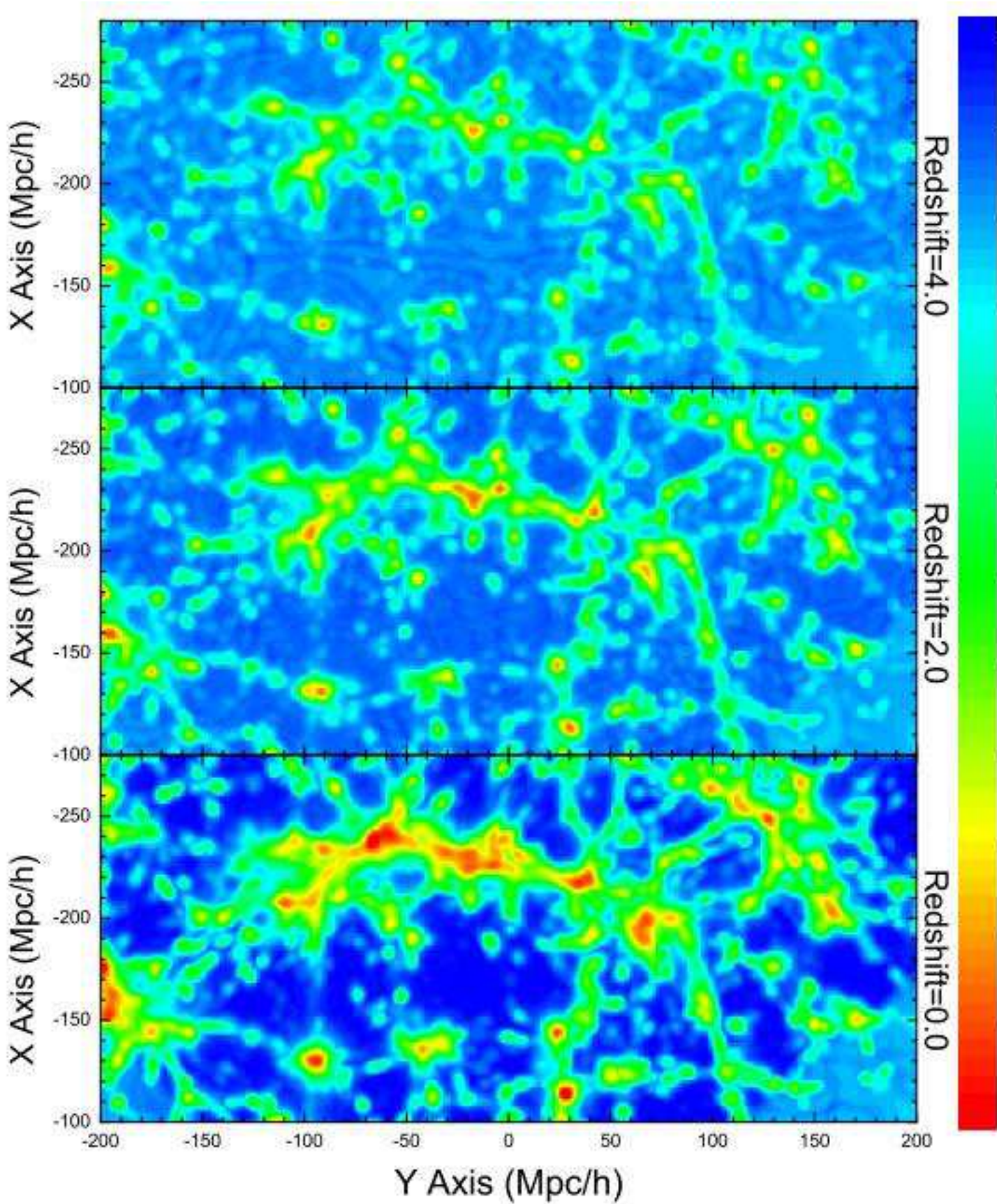


**Figure 13.** The evolution of the density field around the SDSS Great Wall. The density field is produced using Zel'dovich approximation and the predicted velocity field. The color of each grid cell corresponds the logarithm of the density field ( $\log \rho / \bar{\rho}$ ), as indicated in the figure.